AIAA SciTech Forum
8-12 January 2024, Orlando, FL
AIAA SCITECH 2024 Forum
10.2514/6.2024-0794

Investigation of high-frequency thermoacoustic instabilities in a FLOX® burner using large-eddy simulation and multi resolution proper orthogonal decomposition

Andreas Fiolitakis*, Michael Pries†, Oliver Lammel‡ and Trupti Kathrotia§
DLR, Stuttgart, Baden Württemberg, 70569, Germany

In this work we investigate high-frequency thermoacoustic instabilities in a FLOX® gas turbine burner by means of large-eddy simulation (LES). This burner is operated at eight bar pressure with a mixture of hydrogen and natural gas. Experimental data for the pressure oscillations in the combustion chamber are provided here to validate the simulations. The LES is conducted using a splitting scheme for solving the equations for compressible, reactive flows. To model the filtered chemical source terms in LES two different models (namely an assumed probability density function (APDF) model and a thickened flame (TF) model) are used. Time resolved computational data are analyzed using multi resolution proper orthogonal decomposition. It is found that mainly three longitudinal and one mixed transversal-longitudinal modes cause the high-frequency instabilities in the combustor. Computed frequencies of these modes agree excellently with measured frequencies. Amplitudes of the modes are best reproduced by the use of the TF model (the APDF model overestimates the strength of the mixed mode). Further analysis of the computational data obtained with the TF model reveals that the thermodynamic instabilities are caused by an interaction of heat release with hydrodynamic instabilities in the mixing section of the burner.

I. Nomenclature

Latin symbols

a	=	temporal coefficient of MRPOD
c	=	isentropic speed of sound
D_{JC}	=	diameter of jet carrier
E	=	specific total energy
f	=	frequency
I	=	frequency band
j	=	diffusive mass flux
j_t	=	subgrid-scale mass flux
l	=	length scale
$L_1 \dots L_{5+\alpha}$	=	amplitudes of characteristic waves
Ma	=	Mach number
N	=	length of time series
N_s	=	number of species
p	=	pressure
q	=	diffusive heat flux
q_t	=	subgrid-scale heat flux
s	=	entropy
S	=	chemical source term
St_{JC}	=	Strouhal number of jet carrier
t	=	time

*Research Scientist, Institute of Combustion Technology, Computer Simulation Department
†Research Scientist, Institute of Combustion Technology, Computer Simulation Department
‡Head of Department, Institute of Combustion Technology, Department of Combustor Systems and Diagnostics
§Research Scientist, Institute of Combustion Technology, Department of Chemical Kinetics and Analytics

T	=	temperature
u	=	flow velocity
u_n	=	normal flow velocity
$u_{t,1}, u_{t,2}$	=	tangential flow velocities
U_{JC}	=	velocity scale in jet carrier
Y	=	mass fraction
x	=	spatial coordinate

Greek symbols

ζ	=	arbitrary variable
ρ	=	density
$\sigma_2 \ldots \sigma_{5+\alpha}$	=	model parameters of characteristic waves
τ	=	viscous stress tensor
τ_t	=	subgrid-scale stress tensor
ϕ	=	spatial MRPOD mode

Subscripts

α	=	species index
i, j	=	spatial index
k	=	summation index
$trgt$	=	target

Superscripts

$'$	=	fluctuation over time average
$\bar{}$	=	filtered quantity
$\sim$	=	Favre-filtered quantity
T	=	transpose

II. Introduction

The occurrence of thermoacoustic instabilities is a serious problem in technical combustion systems. These type of instabilities are typically caused by a positive feed-back loop between acoustics pressure waves traveling within a combustion device and the unsteady heat release in the combustion chamber. If fluctuations of heat release happen to be "in phase" with pressure oscillations, acoustic energy builds up in the combustion system and pressure oscillations can attain high amplitudes. These pressure waves may modify drastically the flow pattern and subsequently the flame shape and flame position in the combustor which leads usually to unfavorable operating conditions where combustion efficiency declines and pollutant emissions and thermal loads on walls increase. High-frequency pressure oscillations (i.e. frequencies above 1000 Hz [1]) appear to be exceptionally harmful as they can cause high-frequency vibrations in the mechanical structure of the combustion system which lead ultimately to a rapid fatigue of the material. An example of such destructive instabilities is the "screech" phenomenon in aero-engines [2]. The main focus of the present work is, therefore, to further the understanding of such high frequency oscillations in gas turbine combustion through the use of compressible large-eddy simulations (LES). The LES approach is already used extensively for the computation of thermoacoustic instabilities. A review on this topic with emphasis on gas turbine combustion is given in [3] and in particular for rocket engine combustion numerous LES studies exist on high frequency oscillations [4–13]. However, only few studies [1, 14–17] address to our knowledge explicitly the computation of self-excited, high-frequency instabilities (HFI) in gas turbine combustors. The present work extends one of these earlier works which is concerned with scale-adaptive simulations of HFI in a FLOX® gas turbine burner [15]. Compared to [15] an operating point at a higher pressure is considered here and experimental data for pressure in this burner are provided for the first time. These experimental data are used to validate the LES. In addition, the numerical and modeling approach is drastically improved compared to [15] as outlined in Sec. IV. The computational data obtained in this work are analyzed using multi resolution proper orthogonal decomposition (MRPOD) in order to gain insight into the modes of the pressure waves. Results of this analysis are presented in Sec. VI where the thermoacoustic feed-back loop in this burner is also investigated in detail.

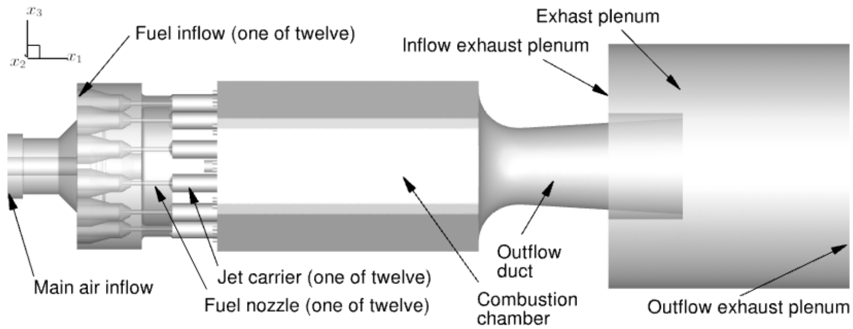

Fig. 1 Solution domain for the LES of the FLOX® gas turbine burner.

III. Test case

A detailed description of the burner which is the subject of the present investigation is given in [15]. The burner is a jet-stabilized, twelve nozzle FLOX® gas turbine burner [18] where high-velocity jets of fuel are mixed with air in jet carriers before they enter the combustion chamber (cf. Fig. 1). The gas mixture discharges with high momentum from the jet carriers into the combustion chamber where it causes exhaust gas recirculation which aides flame stabilization. The combustion chamber (which has a hexagonal shape [19]) is equipped with quartz-glass windows for optical access. The whole burner is mounted into the high pressure test rig HBK-S of the DLR institute of combustion technology where experiments at 8 bar pressure are performed. Details on this test rig are given in [20–23]. The pressure oscillations in the combustion chamber are recorded during the operation of the burner in order to provide validation data for LES. In the present study the burner is fueled with a mixture of hydrogen and natural gas (the mass fractions of hydrogen and natural gas are 22 % and 78 % respectively) at a global equivalence ratio of 0.625 (the air and fuel mass flows amount to 505.88 g/s and 15.74 g/s).

IV. Modeling approach

A. Numerical method

In this work we are interested in solving numerically the Favre-filtered balance equations for mass, momentum, and specific total energy along with the Favre-filtered transport equations of species mass fractions. These equations are given by (Einstein notation)

$$\frac{\partial \bar{\rho}}{\partial t} + \frac{\partial \bar{\rho}\widetilde{u}_i}{\partial x_i} = 0 \ , \tag{1}$$

$$\frac{\partial \bar{\rho}\widetilde{u}_j}{\partial t} + \frac{\partial \bar{\rho}\widetilde{u}_i\widetilde{u}_j}{\partial x_i} = -\frac{\partial \bar{p}}{\partial x_j} + \frac{\partial\left(\bar{\tau}_{ij} + \tau_{t,ij}\right)}{\partial x_i} \ , \tag{2}$$

$$\frac{\partial \bar{\rho}\widetilde{E}}{\partial t} + \frac{\partial}{\partial x_i}\left(\bar{\rho}\widetilde{u}_i\left(\widetilde{E} + \frac{\bar{p}}{\bar{\rho}}\right)\right) = \frac{\partial \widetilde{u}_j\left(\bar{\tau}_{ij} + \tau_{t,ij}\right)}{\partial x_i} - \frac{\partial\left(\bar{q}_i + q_{t,i}\right)}{\partial x_i} \ , \tag{3}$$

$$\frac{\partial \bar{\rho}\widetilde{Y}_\alpha}{\partial t} + \frac{\partial \bar{\rho}\widetilde{u}_i\widetilde{Y}_\alpha}{\partial x_i} = -\frac{\partial\left(\bar{j}_{i\alpha} + j_{t,i\alpha}\right)}{\partial x_i} + \bar{S}_\alpha \ . \tag{4}$$

Here t is the time, x_i the spatial coordinate, ρ the density, p the pressure, u_j the velocity vector, Y_α the mass fraction of the species α (there are a total of $N_s - 1$ linearly independent species, where N_s is the total number of species), and E the specific total energy. τ_{ij} is the viscous stress tensor, q_i the vector of the diffusive heat flux, and $j_{i\alpha}$ and S_α the diffusive mass flux vector and chemical source term of the species α, respectively. It is assumed that the fluid is a mixture of thermally perfect gases and that the equation of state is given by the ideal gas law. Thermodynamic properties are calculated with the approach of [24]. The operator $\bar{\bullet}$ in the above equations denotes a filtered value. A Favre-filtered value $\widetilde{\bullet}$ is defined in terms of filtered quantities as $\widetilde{\bullet} = \overline{(\rho\bullet)}/\bar{\rho}$. The filtering operation of the balance and transport equations leads to the subgrid-scale stress tensor $\tau_{t,ij}$, the subgrid-scale heat flux $q_{t,i}$, and subgrid-scale species mass flux $j_{t,i\alpha}$. Models for these quantities are outlined in Sec. IV.B. To solve Eqs. (1) to (4) we use the implicit characteristic splitting (ICS) approach of [25]. The ICS approach is based on the work of [26, 27] who derive a two step splitting scheme which consists of an advective step followed by an acoustic step. In the ICS approach [25] the equations of the advective step read (Einstein notation)

$$\frac{\partial \bar{\rho}}{\partial t} + \frac{\partial \bar{\rho}\widetilde{u}_i}{\partial x_i} - \bar{\rho}\frac{\partial \widetilde{u}_i}{\partial x_i} = 0 \ , \tag{5}$$

$$\frac{\partial \bar{\rho}\widetilde{u}_j}{\partial t} + \frac{\partial \bar{\rho}\widetilde{u}_i\widetilde{u}_j}{\partial x_i} - \bar{\rho}\widetilde{u}_j\frac{\partial \widetilde{u}_i}{\partial x_i} = \frac{\partial \left(\bar{\tau}_{ij} + \tau_{t,ij}\right)}{\partial x_i} \ , \tag{6}$$

$$\frac{\partial \bar{\rho}\widetilde{E}}{\partial t} + \frac{\partial \bar{\rho}\widetilde{u}_i\widetilde{E}}{\partial x_i} - \bar{\rho}\widetilde{E}\frac{\partial \widetilde{u}_i}{\partial x_i} = \frac{\partial \widetilde{u}_j\left(\bar{\tau}_{ij} + \tau_{t,ij}\right)}{\partial x_i} - \frac{\partial \left(\bar{q}_i + q_{t,i}\right)}{\partial x_i} \ , \tag{7}$$

$$\frac{\partial \bar{\rho}\widetilde{Y}_\alpha}{\partial t} + \frac{\partial \bar{\rho}\widetilde{u}_i\widetilde{Y}_\alpha}{\partial x_i} - \bar{\rho}\widetilde{Y}_\alpha\frac{\partial \widetilde{u}_i}{\partial x_i} = -\frac{\partial \left(\bar{j}_{i\alpha} + j_{t,i\alpha}\right)}{\partial x_i} + \bar{S}_\alpha \ . \tag{8}$$

The equations of the acoustic step of the ICS approach can be expressed as (Einstein notation)

$$\frac{\partial \bar{p}}{\partial t} + \bar{\rho}\bar{c}^2\frac{\partial \widetilde{u}_i}{\partial x_i} = 0 \ , \tag{9}$$

$$\frac{\partial \widetilde{u}_j}{\partial t} + \frac{1}{\bar{\rho}}\frac{\partial \bar{p}}{\partial x_j} = 0 \ , \tag{10}$$

$$\frac{\partial \bar{s}}{\partial t} = 0 \ , \tag{11}$$

$$\frac{\partial \widetilde{Y}_\alpha}{\partial t} = 0 \tag{12}$$

where c denotes the isentropic speed of sound. Note, that the entropy s and the composition Y_α remain constant over time during the acoustic step but they may vary in space. In the ICS scheme [25] a pressure correction method is used as in [26, 27] in order to compute the change in pressure during the acoustic step. Based on the pressure change, the remaining variables are computed. Here, we use a different approach where we solve the hyperbolic equations (9) and (10) directly under the constrains imposed by Eqs. (11) and (12). To this end, we use an implicit weighted averaged flux (WAF) method [28]. The advantage of this approach is that we can ensure monotonicity of the solution which generally is not the case if a pressure correction equation is used. The resulting scheme is termed "ICS-WAF" and is implemented in the in-house code ThetaCOM [29] which is used here to perform the LES.

B. Computational model

To close the system of equations presented in Sec. IV.A, models for the subgrid-scale stress tensor and the subgrid-scale heat and species mass fluxes are required. For the former, we use the wall-adapting local eddy-viscosity (WALE) approach of [30] with a WALE constant of $C_W = 0.1$. The subgrid-scale species mass and energy fluxes are closed using a gradient diffusion approach where the fluxes are related to the gradients of Favre-filtered temperature and Favre-filtered mass fraction. The turbulent diffusivities are computed from the eddy-viscosity by using turbulent Schmidt and Prandtl numbers of 0.7. For the diffusive species mass flux individual species diffusivities are used in a simplified Fickian approach. The thermal conductivity and the molecular viscosity of the gas are computed as mixture averaged values. To close the filtered chemical source $\bar{S}_\alpha$term in Eq. (8) two different model approaches are pursued in this work:

1) An assumed probability density function (APDF) model proposed in [31, 32] is used in one LES. This model requires the solution of two additional transport equations for subgrid-scale temperature variance and the trace of the subgrid-scale species covariance matrix.
2) A thickened flame model (TF) given in [33]. The thickness factor of the model is computed dynamically as suggested in [34], i.e. based on the ratio of the local mesh size and the local thickness of a laminar premixed flame. The latter quantity is obtained here from computations for laminar, freely propagating premixed flames. The flame thickness data are tabulated as function of mixture fraction and for the use in the TF model.

For the simulation the domain shown in Fig. 1 is discretized with an unstructured mesh. On this primary grid a median-dual mesh is created for ThetaCOM which consists of about 10 million control volumes. The computational time step is 0.1 µs. An important aspect is the treatment of in- and outflow boundaries. Here we use the Navier-Stokes characteristic boundary conditions (NSCBC) approach [35]. In the present work the fuel and air inflow boundaries

Table 1 Composition of fuel.

Species	Mass fraction
CH_4	0.626
H_2	0.220
C_2H_6	0.032
CO_2	0.096
N_2	0.026

Table 2 Inflow parameters.

Parameter	Value
σ_2	100 kg/(m s^3 K)
σ_3	100 kg/(m^2 s^2)
σ_4	100 kg/(m^2 s^2)
σ_5	3×10^5 kg/(m^2 s^2)
$\sigma_{5+\alpha}$	100 s^{-1}

Table 3 Outflow parameters.

Parameter	Value
σ_1	3
Ma	0.17
l	0.1075 m
$\bar{p}_{trgt}$	8 bar

are fully reflective since a constant mass flow rate is prescribed at these boundaries. Temperature and composition are taken to be constant at these inflow boundaries: The air temperature is 673.1 K, the fuel temperature is 343.4 K. The composition of the fuel is given in Tab. 1, for air we assume an oxygen mass fraction of 0.23 and a nitrogen mass fraction of 0.77. The inflow and outflow of the exhaust plenum depicted in Fig. 1 are non-reflective. The amplitudes of the incoming characteristic waves, i.e. L_2 to $L_{5+\alpha}$, are modeled at the non-reflective inflow boundaries as [35–37]

$$L_2 = \sigma_2 \, (\widetilde{T} - \widetilde{T}_{trgt}) \ , \tag{13}$$
$$L_3 = \sigma_3 \, (\widetilde{u}_{t,1} - \widetilde{u}_{t,1,trgt}) \ , \tag{14}$$
$$L_4 = \sigma_4 \, (\widetilde{u}_{t,2} - \widetilde{u}_{t,2,trgt}) \ , \tag{15}$$
$$L_5 = \sigma_5 \, (\widetilde{u}_n - \widetilde{u}_{n,trgt}) \ , \tag{16}$$
$$L_{5+\alpha} = \sigma_{5+\alpha} \, (\widetilde{Y}_\alpha - \widetilde{Y}_{\alpha,trgt}) \ . \tag{17}$$

In these equations T denotes the temperature, and the vector $\left(u_n, u_{t,1}, u_{t,2}\right)^T$ is the velocity vector at the boundary (the coordinates of this velocity vector are expressed for each boundary face in a local coordinate system which is aligned with the normal vector of a boundary face). The index $trgt$ denotes target quantities which have to be specified. For the target temperature and target composition we assume an adiabatic-isobaric chemical equilibrium (i.e. for an air-fuel mixture at an equivalence ratio of 0.625 and a pressure of 8 bar). The target normal velocity $u_{n,trgt}$ is set to 40 m/s, the tangential velocity components $u_{t,1,trgt}$ and $u_{t,2,trgt}$ to 0 m/s. The model parameters σ_2 to $\sigma_{5+\alpha}$ are summarized in Tab. 2. For the outflow of the exhaust plenum only one characteristic wave amplitude needs to be specified, i.e.

$$L_1 = \sigma_1 \left(1 - Ma^2\right) \frac{\bar{c}}{l} \left(\bar{p} - \bar{p}_{trgt}\right) \tag{18}$$

where the approach of [38] is used. The parameters for the outflow boundary (i.e. Mach number Ma, length scale l, target pressure $\bar{p}_{trgt}$ and model parameter σ_1) are given in Tab. 3. All wall boundaries are acoustically fully reflective. They are assumed to be adiabatic with exception of the combustion chambers walls. For the side walls forming the hexagon and the outflow duct a constant temperature of 800 K is assumed. At the base plate of the combustion chamber a constant temperature of 766.44 K is used (this value is obtained from measurements).

C. Reaction mechanism

An important aspect in this LES is the reaction mechanism used to describe the oxidation of the hydrogen-natural gas mixture. The natural gas itself is a mixture of various gases. Its approximate composition is given in Tab. 1 in terms of mass fractions. It appears to contain about 3 % C_2H_6. Hence, a reaction mechanism is required which accurately describes the C2-chemistry as well as the chemistry of CH_4-H_2 mixtures. To this end a reduced reaction mechanism is derived in this work from the DLR Concise reaction mechanism [39]. During the reduction process the reaction mechanism is validated against experimental data: Ignition delay times as well as laminar flame speeds of C_2H_6 and various mixtures of H_2 and CH_4 are considered at pressures ranging from 1 atm up to 60 atm. The resulting mechanism consists of 25 species and 126 reactions.

V. MRPOD method

In this work the MRPOD method [40, 41] is used to analyze the computational data. The MRPOD approach is motivated by the fact that conventional proper orthogonal decomposition (POD) identifies spatial mode solely by their

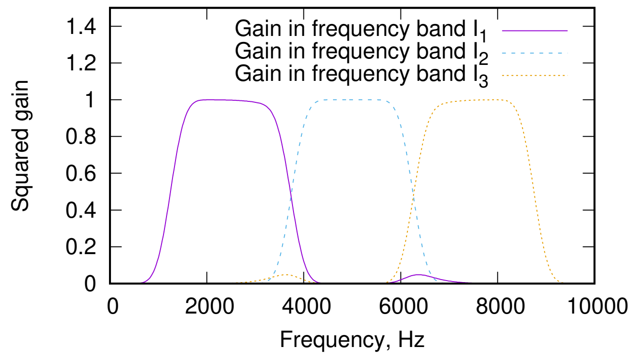

Fig. 2 Squared gain of filters in MODPWT.

energy content. It may therefore miss modes which are important to the dynamics of a variable but which have at the same time a relatively low energy content. The MRPOD of [40, 41] overcomes this problem by incorporating a multiresolution analysis on the basis of wavelets (i.e. the cross correlation matrix of a variable is decomposed using wavelets before computing the POD). In this way a unique frequency band of a variable is considered in the spectral domain. Formally, the MRPOD of a variable $\zeta(x_i, t)$ in a frequency band I is expressed as

$$\zeta(x_i, t)'_I \quad = \quad \sum_{k=1}^{N} a_{k,I}(\zeta, t)\ \phi_{k,I}(\zeta, x_i) \tag{19}$$

where N denotes the length of the time series, $a_{k,I}(\zeta, t)$ the kth temporal coefficient in the frequency band I, and $\phi_{k,I}(\zeta, x_i)$ the corresponding spatial mode. The operator $\bullet'$ denotes the fluctuation of a variable over its time average given by the operator $\langle\bullet\rangle$, i.e.

$$\zeta(x_i, t) \quad = \quad \langle\zeta(x_i, t)\rangle + \zeta(x_i, t)' \ . \tag{20}$$

In the present work we follow [41] and use maximum overlap discrete packet wavelet transform (MODPWT) and employ Daubechies least asymmetric wavelet [42] with twelve basis elements and a decomposition level of three. We use the first, third, and fifth scale of this MODPWT and employ a total of two scales. The squared gain of the resulting bandpass filter is shown in Fig. 2. The filters cover the nominal frequency bands I_1 = [1717 Hz; 3100 Hz], I_2 = [4218 Hz; 5782 Hz], and I_3 = [6700 Hz; 8400 Hz] which is the relevant frequency range for HFI in this burner as discussed in Sec. VI.

VI. Results

A. Frequency spectrum

To assess the fidelity of the two different models for the filtered chemical source term (i.e. the APDF and the TF model) we investigate in a first step the pressure in the combustion chamber. The relative pressure computed with these two models is shown in Fig. 3. The results are normalized with the operating pressure of 8 bar. Both computations are started from a reactive LES which is performed with an incompressible pressure correction method (i.e. compressibility is neglected in this initial solution). In both computations the pressure oscillations grow initially exponentially over time where a large growth rate is observed in the LES with the APDF model. In contrast to that the pressure amplitudes computed with the TF model grows first slower over time but increases rapidly after approximately 0.02 s. The amplitude reaches maximal values between 0.03 s and 0.04 s where an “overshoot zone” is observed. This “overshoot zone” is followed by a limit cycle where pressure amplitude remains constant. Such an “overshoot zone” is missing in the LES with the APDF model. Instead, after approximately 0.035 s the exponential amplitude growth of the pressure amplitude ceases and the amplitude oscillations enter a limit cycle. Compared to the simulation with the TF model the amplitude of the APDF model appears to be about 45 % higher in the limit cycle. The measured normalized pressure is shown in Fig. 4. A direct comparison of Figs. 3 and 4 shows that the measured amplitudes are about 2.75 time lower than the computed amplitudes of the TF model and even four times lower than the computed amplitudes of the APDF model.

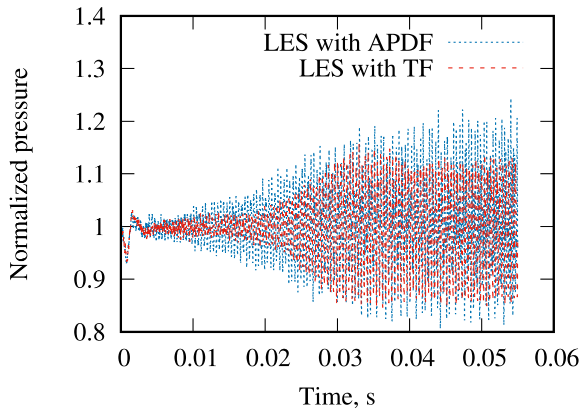

Fig. 3 Normalized computed pressure.

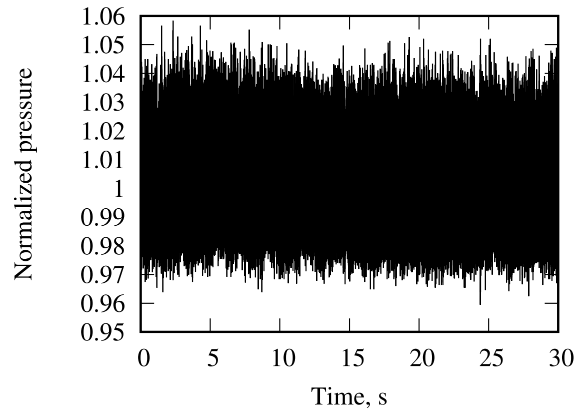

Fig. 4 Normalized measured pressure.

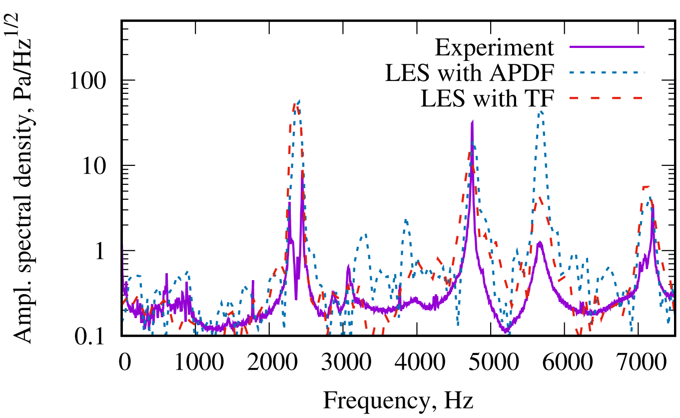

Fig. 5 Amplitude spectral density of pressure in the combustion chamber.

This overestimation of amplitudes by both computations is reflected in the amplitude spectral density (ASD) of pressure which is shown in Fig. 5. The frequencies of the four major “peaks” observed in the experiment, i.e. 2390 Hz, 4770 Hz, 5670 Hz, and 7199 Hz, are captured extremely well by LES with both the APDF and TF model. Also the amplitudes of the modes at 4770 Hz and 7199 Hz are computed accurately by both models. The amplitude of the first mode at 2390 Hz is, however, clearly overestimated by both models. A noteworthy discrepancy between both LES and experiment is the occurrence of a double peak in the experiment close to 2390 Hz. This peak is not reproduced by either LES. A closer analysis of the experimental data reveals that both modes are simultaneously present in the measured pressure, i.e. no switching between two frequencies occurs. A possible explanation why this double peak is not observed in LES is presented in Subsec. VI.C. At 5670 Hz there appears to be a big difference between the results of the models. The amplitude of this mode is well reproduced by the LES with the TF model. The LES with the APDF model overestimates the amplitude by a large factor of almost 100. Since the LES with the TF model appears to give the better agreement to available experimental data we focus the following investigations on the results of this particular LES.

B. Averaged fields of LES with TF model

To provide an impression of the flow field within the combustor streamlines are shown in Fig. 6 for the LES with the TF model along with contour plots of average OH mass fraction, average temperature, average heat release, and average u_1 velocity. The computations have been run for 55 ms which corresponds to about 7.8 through flow times. The data shown in Fig. 6 are extracted in a plane at $x_2 = 0.011$ m (the orientation of the coordinate system is shown in Fig. 1, the origin is located at the center of the combustion chamber’s base plate). It is clear from Fig. 6 that a recirculation zone is formed within the combustion chamber which transports continuously hot combustion products back to the root of the flame and thus aids its stabilization. On average the flame appears to be anchored at the exit of the jet carrier as the heat

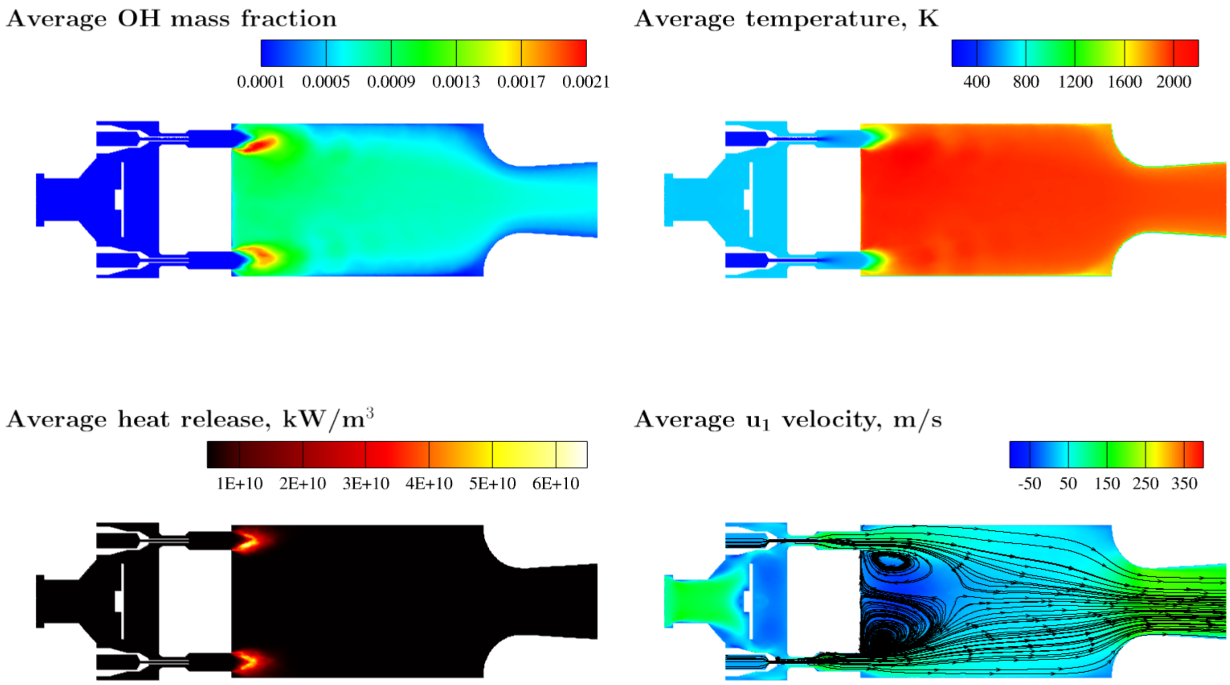

Fig. 6 Averaged fields of OH mass fraction, temperature, heat release, and u_1 velocity (LES with TF model).

release indicates.

C. Analysis of pressure modes for LES with TF model

To elucidate the modes associated with the four frequencies presented in Sec. VI.A we perform an MRPOD of the computed pressure field as described in Sec. V. Results for the spatial pressure modes $\phi_{k,I}(p)$ in each of the frequency bands I_1, I_2, and I_3 are given in Fig. 7. The first modes, i.e. $\phi_{1,I_1}(p)$, $\phi_{1,I_2}(p)$, and $\phi_{1,I_3}(p)$ contain most of the energy in these frequency bands as an examination of the relative energy content in Fig. 9 reveals. They contain between 57 % and 94 % of the energy. These three modes are purely longitudinal modes in the combustion chamber and outflow duct, where $\phi_{1,I_2}(p)$ and $\phi_{1,I_3}(p)$ are the second and third harmonic of $\phi_{1,I_1}(p)$. The frequencies of these three modes can be deduced from the Fast Fourier transforms (FFT) of the temporal coefficients $a_{1,I_1}(p)$, $a_{1,I_2}(p)$, and $a_{1,I_3}(p)$ which is given in Fig. 8. It appears that the mode $\phi_{1,I_1}(p)$ oscillates at a frequency of 2390 Hz whereas $\phi_{1,I_2}(p)$ and $\phi_{1,I_1}(p)$ oscillate at frequencies of 4770 Hz and 7199 Hz. Hence, the HFI observed experimentally at these three frequencies are attributed to purely longitudinal modes. As shown in Fig. 8 the modes $\phi_{2,I_1}(p)$ and $\phi_{2,I_2}(p)$ contribute also to the HFI at 2390 Hz and 4770 Hz. The mode $\phi_{2,I_1}(p)$ causes mainly HFI in the air plenum. It could be due to such a plenum mode that two modes are observed experimentally at 2390 Hz as shown in Fig. 5. In the MRPOD of the LES data it is found that such a plenum mode may still cause low amplitude pressure oscillations in the combustion chamber. The frequency of such a mode might depend on the modeling of the inflow boundary condition for the main air flow. In the LES presented here, we use a fully reflective inflow boundary condition as outlined in Sec. IV.B. The use of a partially reflective inflow boundary might modify the frequency of this mode in such a way that two modes are ascertainable at 2390 Hz. Such a hypothesis requires, however, still verification. The mode $\phi_{2,I_2}(p)$ entails also a HFI in the plenum which appears to be first harmonic of $\phi_{2,I_1}(p)$ at a frequency of 4770 Hz. In addition, HFI are observed in the outflow duct as well as in the jet carriers. Both of these modes have, however, a relatively low energy content compared to the first modes as shown in Fig. 9 (approx. 6 % for $\phi_{2,I_1}(p)$ and approx. 20 % for $\phi_{2,I_2}(p)$). An exception to the aforementioned modes is the mode $\phi_{3,I_2}(p)$. This mode has a very low energy content compared to the modes 1 and 2 in the frequency band I_2. Its energy content amounts to about 2 %. This mode, however, is mainly responsible for the HFI

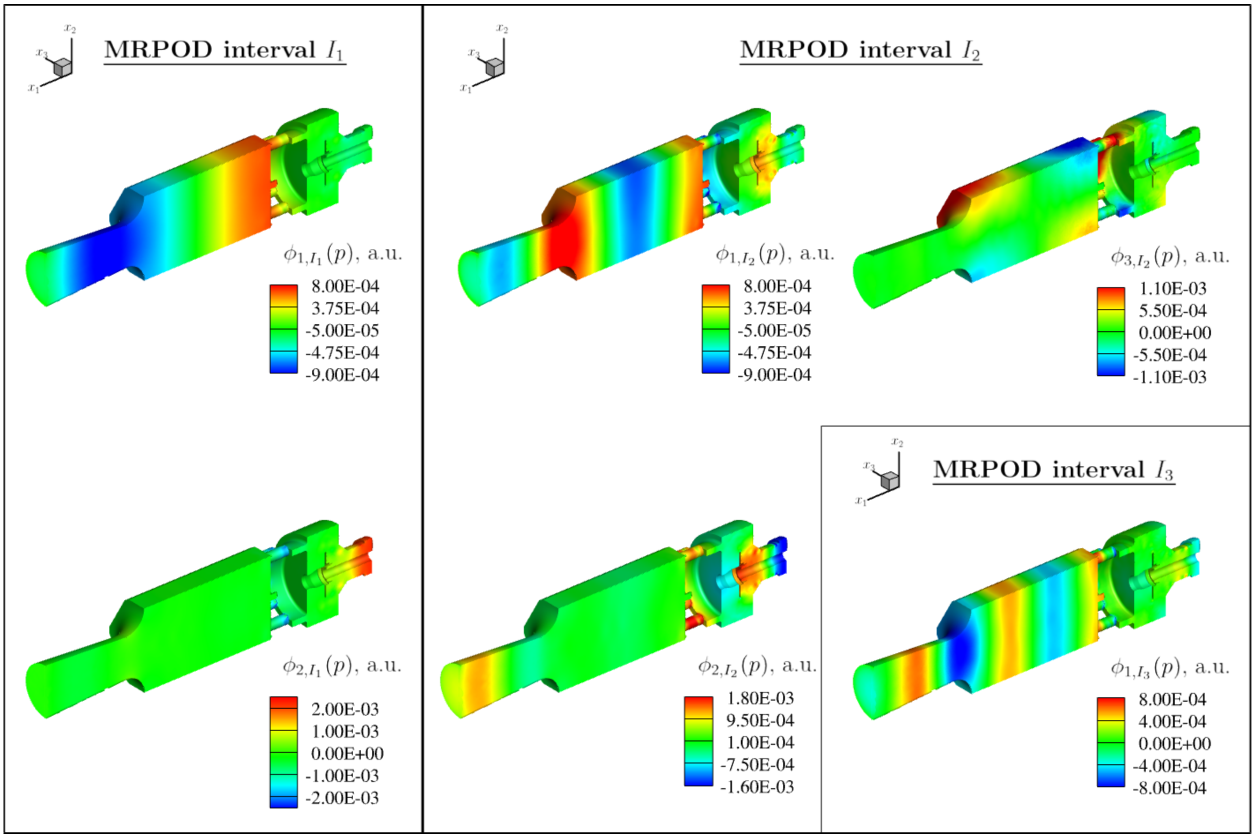

Fig. 7 MRPOD modes in burner. The data are extracted from LES with TF model.

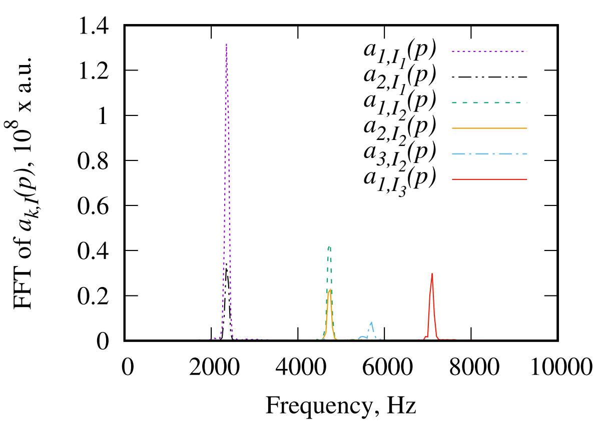

Fig. 8 FFT of the time coefficients.

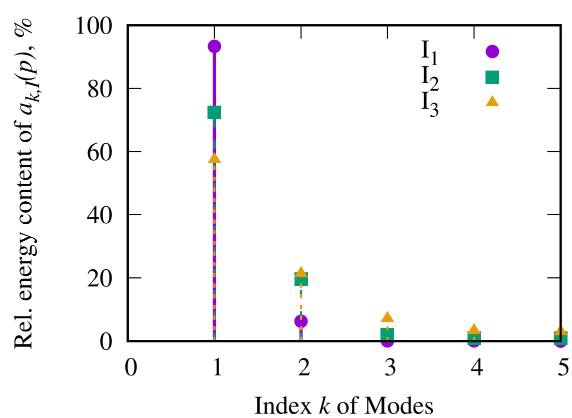

Fig. 9 Relative energy content.

observed at 5670 Hz as the FFT of $a_{3,I_2}(p)$ in Fig. 8 shows. Compared to the other MRPOD modes $\phi_{3,I_2}(p)$ is a mixed transverse-longitudinal mode. Its position appears to be stationary, i.e. no spinning in transversal direction is found here (spinning requires a pair of modes which is not found here). It is for this particular mixed transverse-longitudinal mode that the biggest differences between the LES with the APDF and TF model are found in Fig. 5. For the present configuration it seems, therefore, that the computation of mixed HFI mode is particularly sensitive to the closure of the chemical source term in Eq. (8).

D. Investigation of thermoacoustic feed-back loop in LES with TF model

In order to further the understanding of HFI in this burner, we investigate the thermoacoustic feed-back loop between heat release and pressure oscillations with help of the LES with the TF model. We consider first the average spatial distribution of heat release in the combustion chamber. To this end we plot in Fig. 10 the average heat release on a cylindrical surface which intersects the jet carriers and the fuel nozzle. In contrast to Fig. 6 (where only two nozzles are shown in a planar contour plot) the left illustration in Fig. 10 clearly reveals in the spatial distribution of average heat release a rotational symmetry about the x_1 axis. For each flame anchoring at the exit of a jet carrier, the maximum heat release is found on a side denoted by “C” in the right illustration of Fig. 10. In the right illustration of Fig. 10 isolines of the average heat release are shown where they are superimposed on a contour plot of the average u_1 velocity field. It appears that the average u_1 velocity field follows the same rotational symmetry about the x_1 axis. At the entrance of each jet carrier two opposite sharp edges exist as shown in Fig. 10 where flow separation bubbles denoted by “A” and “B” are formed. These flow separation bubbles have different sizes. The larger one is located in point “B”, i.e. on the same side as point “C” where the maximum heat release is found. The larger size of the separation bubble in point “B” can be explained by the retarding effect of the large heat release in point “C”. The large heat release in point “C” leads to a strong dilatation of the velocity field due to thermal expansion of the gases [43]. Due to this effect the gas velocities ahead of point “C” are reduced which promotes the flow separation in point “B”. A further consequence of this flow dilatation in point “C” is that the flow is being diverted towards the edge opposite of “C”. This leads to an increased velocity in the area denoted by “D” in Fig. 10. This increase in flow velocity in the area “D” is accompanied by a reduction of heat release in this area (compared to the point “C”). Thus, the oncoming flow from edge

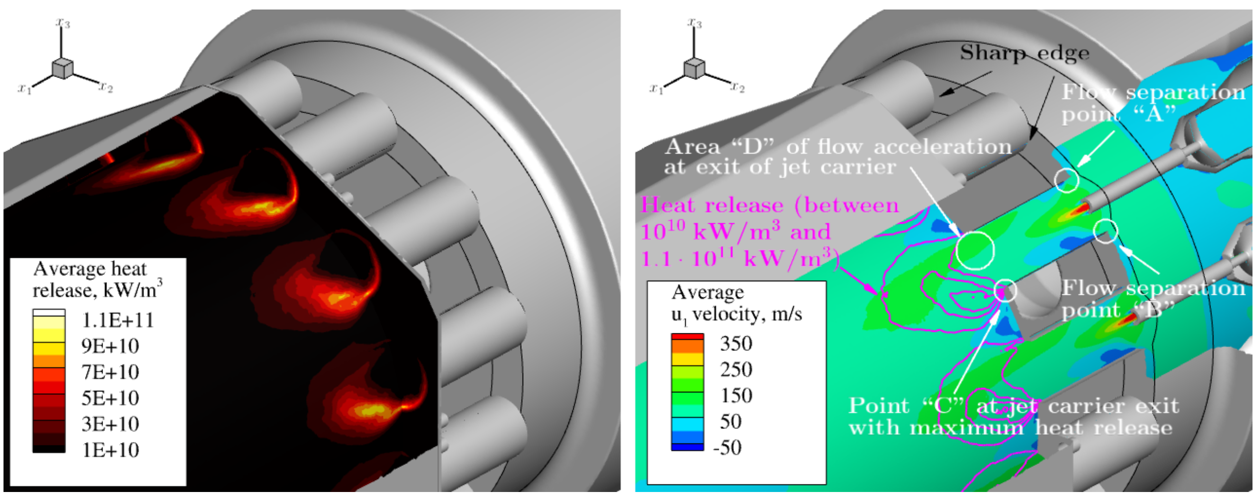

Fig. 10 Average heat release and u_1 velocity in combustion chamber.

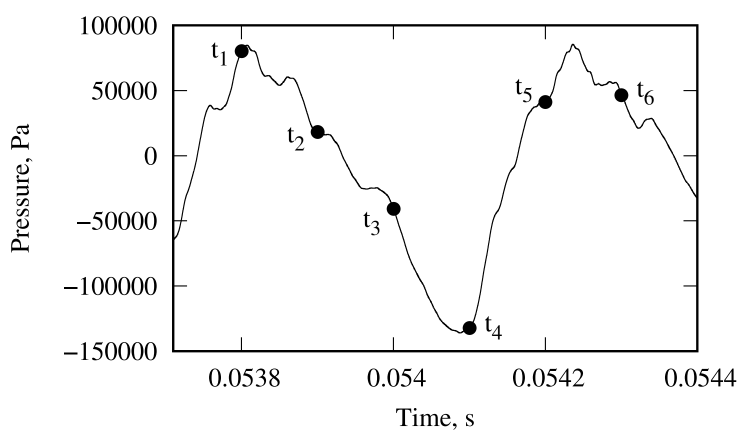

Fig. 11 Pressure in combustion chamber during one thermoacoustic cycle (obtained from LES with TF model).

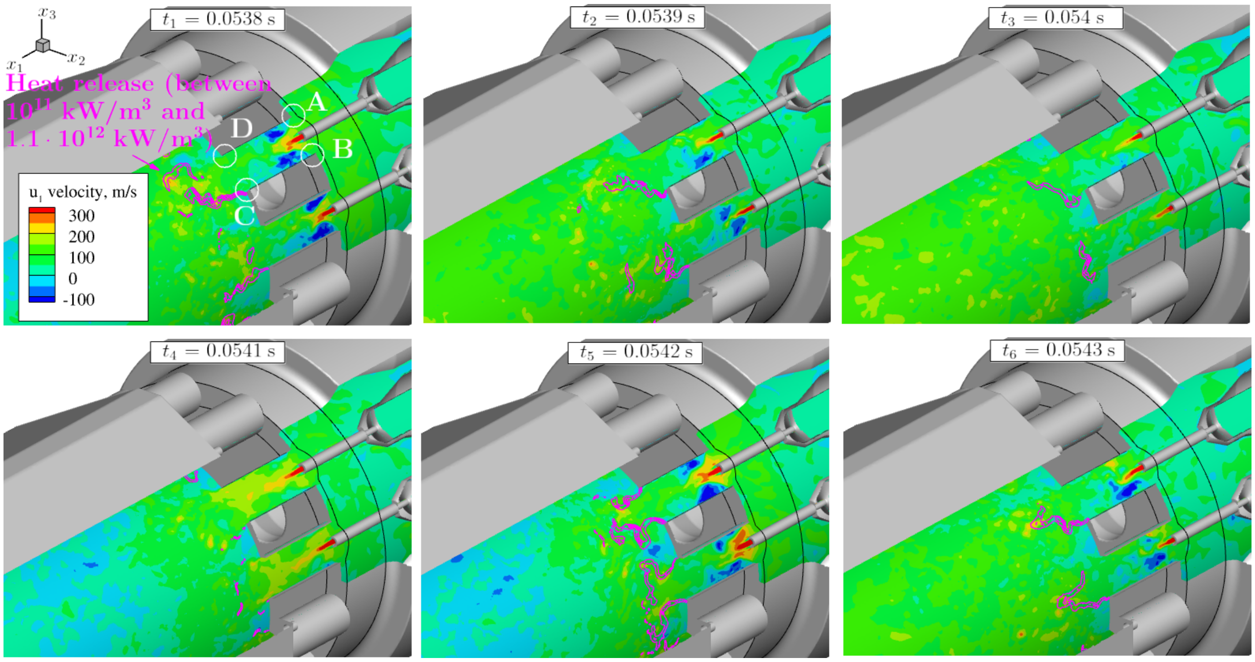

Fig. 12 Instantaneous heat release and u_1 velocity in combustion chamber during one pressure oscillation in the limit cycle. The pressure in the combustion chamber at each time instance is given in Fig. 11.

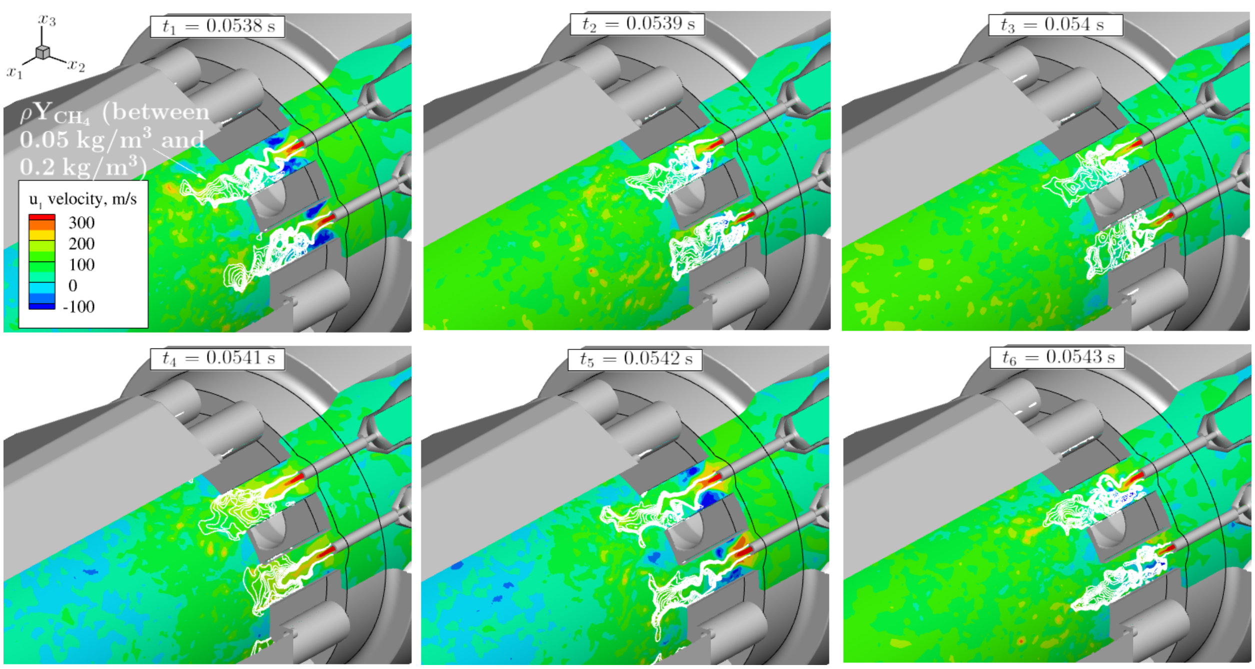

Fig. 13 Instantaneous mass density of methane and u_1 velocity in combustion chamber during one pressure oscillation in the limit cycle. The pressure in the combustion chamber at each time instance is given in Fig. 11.

"A" meets less flow resistance and consequently the separation bubble is smaller compared to the one in point "B". This interaction between the flow separation bubble (i.e. a hydrodynamic instability) and heat release appears to be the main feed-back mechanism in this LES of the burner. The rotational symmetry in heat release might also be the reason for the occurrence of transversal modes in this burner. To show the interaction between heat release and flow separation in more detail both the instantaneous heat release and the instantaneous u_1 velocity are evaluated over the duration of a single pressure oscillation. Such an oscillation is shown in Fig. 11. In this figure different points in time denoted by t_1 to t_6 are highlighted which cover different phases of the pressure oscillation. Instantaneous images of heat release and u_1 velocity are shown in Fig. 12 for each of these points in time. At time t_1 the cycle begins in a pressure maximum and we observe two separation bubbles in point "A" and "B". At this point in time the largest heat release occurs in the proximity of point "C" and the separation bubble in point "B" is larger compared to point "A" (it almost extends to point "C"). The flow conditions at point "B" and "C" interact with each other. The large heat release in point "C" favors on one hand the strong flow separation in point "B". On the other hand, the flow separation in point "B" reduces the flow velocity of the incoming flow in point "C" and provides favorable conditions for flame anchoring. Hence, the flame is located preferably in the proximity of point "C". On the opposite side at point "D" the flow velocities appear to be higher thus favoring flame blow-off. Due to absence of strong flow dilatation in point "D", the separation bubble in point "A" is also comparatively small. Thus, the flow conditions in the points "A" and "D" also affect each other. This flow pattern prevails for the times t_2 and t_3. The maximum heat release is observed in the proximity of point "C" which explains why on average the maximum heat release is found on this side. At time t_4 the pressure in the combustion chamber reaches its minimum (cf. Fig. 11) and the u_1 velocity in the jet carrier reaches its maximum value due to the large pressure gradient across the jet carrier. At this point in time the flame is almost completely blown-off and the separation bubbles are diminished in size as the flow attaches to the walls. As the flow is forced to attach to the wall, the flow passing the sharp edges in "A" and "B" experiences strong centrifugal forces and begins again to separate. For this reason we observe again in the time point t_5 the formation of separation bubbles at both edges. Strong heat release appears now temporarily both in the points "C" and "D" and the pressure in the combustion chamber increases. In the time point t_6 the whole cycle starts from the beginning. To demonstrate that the thermoacoustic is mainly based on the

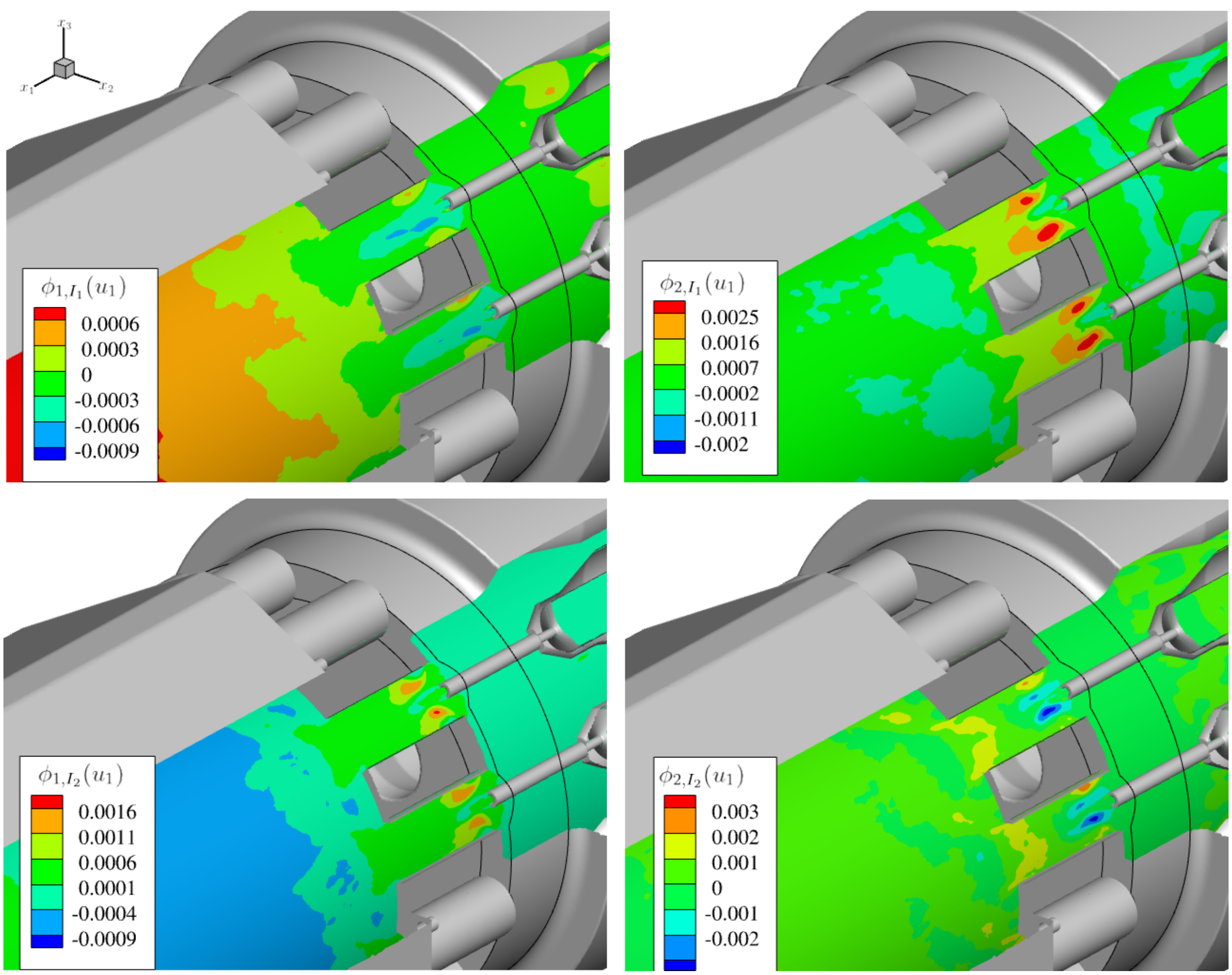

Fig. 14 MRPOD modes of u_1 velocity in combustion chamber.

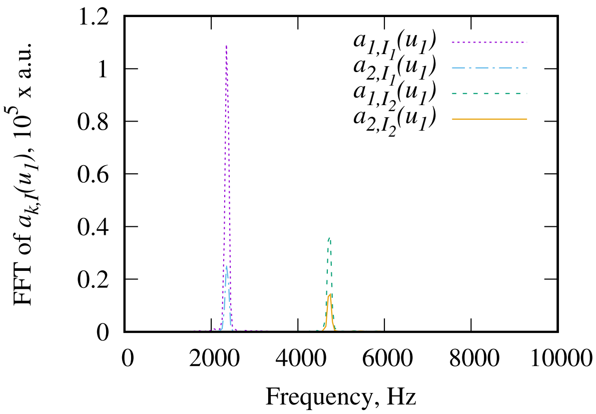

Fig. 15 FFT of the time coefficients.

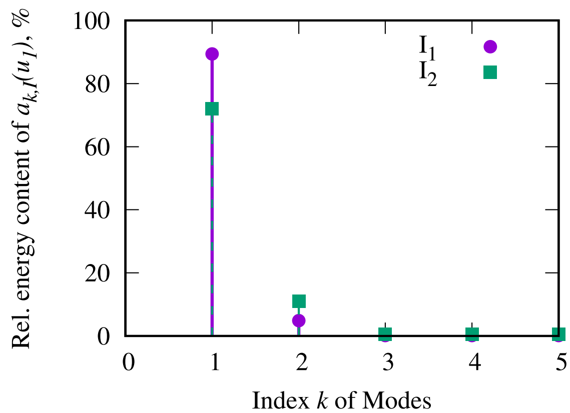

Fig. 16 Relative energy content.

interaction of heat release and a hydrodynamic instability the mass density of methane (i.e. $\rho Y_{\mathrm{CH_4}}$) is shown in Fig. 13 over the entire cycle defined in Fig. 11. Compared to heat release the distribution of fuel appears to be less affected by the dynamics of the flow field since the mixing of the fuel jet is extremely efficient in this type of burner. In a final step we investigate also the the dynamics of the u_1 velocity field with the help of MRPOD. Results for different modes in the frequency bands I_1 and I_2 are summarized in Fig. 14, the FFT of the temporal coefficients and the relative energy content for each mode are summarized in Figs. 15 and 16. Due to the strong pressure oscillations most of the energy is concentrated in the first modes $\phi_{1,I_1}(u_1)$ and $\phi_{1,I_2}(u_1)$. The hydrodynamic instabilities in the region of the jet carrier are contained in the second MRPOD modes $\phi_{2,I_1}(u_1)$ and $\phi_{2,I_2}(u_1)$. From the contour plot in Fig. 14 it is clear that the dynamics of the separation bubble are mainly contained in $\phi_{2,I_1}(u_1)$. In this illustration the different sizes of the separation bubbles can be clearly ascertained. Furthermore, it is also clear that the dynamics of the separation bubble affect the flow field up to the exit of the jet carrier and affect thus the stabilization of the flame. The frequency f of the separation is found to equal 2390 Hz, i.e. the frequency of the first transversal mode. This corresponds to a diameter based jet carrier Strouhal number of $St_{JC} = f\ D_{JC}/U_{JC} \approx 0.24$ (for a jet carrier velocity scale U_{JC} = 120 m/s and a jet carrier diameter D_{JC} = 0.012 m). This dimensionless frequency equals typical values found in other flows with hydrodynamic instabilities (e.g. flows in a pipe bent [44]).

VII. Summary and Conclusions

In the present work compressible LES of reactive flow is used to investigate HFI in a jet-stabilized, twelve nozzle FLOX® gas turbine burner which is operated at 8 bar at globally lean conditions with a mixture of hydrogen and natural gas. The set of governing equations is solved numerically using the ICS-WAF method. In- and outflow boundary conditions are handled via the NSCBC approach. LES results obtained with two different models for the filtered chemical source term, namely an APDF and a TF model, are compared to experimental data for pressure which are obtained in this work for the first time in this burner. Since the LES with the TF model appears to give a good agreement to available experimental data the results of this LES are analyzed further in order to understand the thermoacoustic feed-back cycle. The results of this work may be summarized as follows:

1) It is found in the experiments that HFI occur at four frequencies of 2390 Hz, 4770 Hz, 5670 Hz, and 7199 Hz. These frequencies are reproduced accurately by the compressible LES with both the APDF and TF model.
2) Using MRPOD to analyze the computational data it is found that the frequencies of 2390 Hz, 4770 Hz, and 7199 Hz are associated with a longitudinal mode in the combustion chamber and its higher harmonics whereas the frequency of 5670 Hz corresponds to the first mixed transverse-longitudinal mode in the combustion chamber.
3) The measured amplitudes of the HFI appear to be well reproduced by the use of the TF model with exception of the amplitude of the first longitudinal mode at 2390 Hz which is overestimated. The APDF model largely overestimates the amplitude of the mixed transverse-longitudinal mode at 5670 Hz as well as the amplitude of the first longitudinal mode at 2390 Hz. It is therefore concluded that for the present burner the choice of model for the filtered chemical source term is crucial for capturing correctly the amplitudes of transverse HFI modes.
4) Analysis of the thermoacoustic feed-back reveals that the HFI is mainly caused by an interaction of flow separation

bubbles at the entrance to the jet carrier and the heat release zone at jet carriers exit. The mixing of fuel and air does not appear to play a significant role in this feed back. Hence, according to LES data the interaction of the flame with a hydrodynamic instability appears to be the main driver for HFI. Suppressing the hydrodynamic instabilities through geometric modifications of the jet carrier might therefore be a way of avoiding HFI in this burner.

5) In LES it is found that the heat release zone has a rotational symmetry about the burner axis. It seems, therefore, that this rotational symmetry is the main cause for triggering transversal modes.

References

[1] Bonnaire, P., and Polifke, W., "Analysis of high-frequency dynamics of a reacting jet in crossflow based on large eddy simulation," *Journal of Engineering for Gas Turbines and Power*, Vol. 146, 2023, p. 031002.

[2] Rogers, D., and Marble, F., "A Mechanism for high-frequency oscillation in ramjet combustors and afterburners," *Journal of Jet Propulsion*, Vol. 26, 1956, pp. 456–462.

[3] Poinsot, T., "Prediction and control of combustion instabilities in real engines," *Proceedings of the Combustion Institute*, Vol. 36, 2017, pp. 1–28.

[4] Matsuyama, S., Shinjo, J., Ogawa, S., and Mizobuchi, Y., "Large eddy simulation of high-frequency combustion instability of supercritical LO_x/GH_2 flame," *Proceedings of the 46th AIAA/ASME/SAE/ASEE Joint Propulsion Conference*, 2010. Paper No: AIAA2010-6567.

[5] Matsuyama, S., Shinjo, J., and Mizobuchi, Y., "LES of high-frequency combustion instability in a rocket combustor," *Proceedings of the 51st AIAA Aerospace Sciences Meeting including the New Horizons Forum and Aerospace Exposition*, 2013. Paper No: AIAA2013-0564.

[6] Garby, R., Selle, L., and Poinsot, T., "Large-eddy simulation of combustion instabilities in a variable-length combustor," *Comptes Rendus Mecanique*, Vol. 341, 2013, pp. 220–229.

[7] Hakim, L., Ruiz, A., Schmitt, T., Boileau, M., Staffelbach, G., Ducruix, S., Cuenot, B., and Candel, S., "Large eddy simulations of multiple transcritical coaxial flames submitted to a high-frequency transverse acoustic modulation," *Proceedings of the Combustion Institute*, Vol. 35, 2015, pp. 1461–1468.

[8] Hakim, L., Schmitt, T., Ducruix, S., and Candel, S., "Dynamics of a transcritical coaxial flame under a high-frequency transverse acoustic forcing: Influence of the modulation frequency on the flame response," *Combustion and Flame*, Vol. 162, 2015, pp. 3482–3502.

[9] Urbano, A., Selle, L., Staffelbach, G., Cuenot, B., Schmitt, T., Ducruix, S., and Candel, S., "Exploration of combustion instability triggering using Large Eddy Simulation of a multiple injector liquid rocket engine," *Combustion and Flame*, Vol. 169, 2016, pp. 129–140.

[10] Urbano, A., Douasbin, Q., Selle, L., Staffelbach, G., Cuenot, B., Schmitt, T., Ducruix, S., and Candel, S., "Study of flame response to transverse acoustic modes from the LES of a 42-injector rocket engine," *Proceedings of the Combustion Institute*, Vol. 36, 2017, pp. 2633–2639.

[11] Urbano, A., and Selle, L., "Driving and damping mechanisms for transverse combustion instabilities in liquid rocket engines," *Journal of Fluid Mechanics*, Vol. 820, 2017, p. R2.

[12] Schmitt, T., Staffelbach, G., Ducruix, S., Gröning, S., Hardi, J., and Oschwald, M., "Large-Eddy Simulations of a sub-scale liquid rocket combustor: influence of fuel injection temperature on thermo-acoustic stability," *Proceedings of the 7th European Conference for Aeronautics and Aerospace Sciences (EUCASS)*, 2017.

[13] Morii, Y., Beinke, S., Hardi, J., Shimizu, T., Kawashima, H., and Oschwald, M., "Dense core response to forced acoustic fields in oxygen-hydrogen rocket flames," *Propulsion and Power Research*, Vol. 9, 2020, pp. 197–215.

[14] Ghani, A., Poinsot, T., Gicquel, L., and Staffelbach, G., "LES of longitudinal and transverse self-excited combustion instabilities in a bluff-body stabilized turbulent premixed flame," *Combustion and Flame*, Vol. 162, 2015, pp. 4075–4083.

[15] Grimm, F., Lourier, J., Lammel, O., Noll, B., and Aigner, M., "A selective fast fourier filtering approach applied to highfrequency thermoacoustic instability analysis," *Proceedings of ASME Turbo Expo*, 2017. Paper No: GT2017-63234.

[16] Sharifi, V., Beck, C., Janus, B., and Kempf, A., "Design and testing of a high frequency thermoacoustic combustion experiment," *AIAA Journal*, Vol. 59, 2021, pp. 3127–3143.

[17] Jella, S., Füri, M., and Katsapis, V., "Numerical analysis of high frequency transverse instabilities in a can-type combustor," *Proceedings of ASME Turbo Expo*, 2023. Paper No: GT2023-103298.

[18] Lammel, O., Schütz, H., Schmitz, G., Lückerath, R., Stöhr, M., Noll, B., Aigner, M., Hase, M., and Krebs, W., "FLOX® combustion at high power density and high flame temperatures," *Journal of Engineering for Gas Turbines and Power*, Vol. 132, 2010, p. 121503.

[19] Fiolitakis, A., Lückerath, R., Lammel, O., Schmitz, G., Ax, H., Stöhr, M., Arndt, C., Noll, B., and Kluß, D., "Assessment of a finite-rate-chemistry model for ANSYS®CFX®using experimental data of a downsized gas turbine combustor," *Proceedings of the ASME Turbo Expo*, 2018. Paper no. GT2018-75638.

[20] Fleck, J., Griebel, P., Steinberg, A., Stöhr, M., Aigner, M., and Ciani, A., "Experimental investigation of a generic, fuel flexible reheat combustor at gas turbine relevant operating conditions," *Proceedings of the ASME Turbo Expo*, 2010. Paper no. GT2010-22722.

[21] Ax, H., Stopper, U., Meier, W., Aigner, M., and Güthe, F., "Experimental analysis of the combustion behavior of a gas turbine burner by laser measurement techniques," *Journal of engineering for gas turbines and power*, Vol. 132, 2010, pp. 051503–1 – 051503–9.

[22] Lückerath, R., Lammel, O., Stöhr, M., Boxx, I., Stopper, U., Meier, W., Janus, B., and Wegner, B., "Experimental investigations of flame stabilization of a gas turbine combustor," *Proceedings of the ASME Turbo Expo*, 2011. Paper no. GT2011-45790.

[23] Lammel, O., Severin, M., Ax, H., Lückerath, R., Tomasello, A., Emmi, Y., Noll, B., Aigner, M., and Panek, L., "High momentum jet flames at elevated pressure, A: Experimental and numerical investigation for different fuels," *Proceedings of the ASME Turbo Expo*, 2017. Paper no. GT2017-64615.

[24] McBride, J., Gordon, S., and Reno, M., "Coefficients for calculating thermodynamic and transport properties of individual species," Technical Report NASA Technical Memorandum 4513, NASA, NASA, Lewis Research Center, Cleveland Ohio, 1993.

[25] Pries, M., Fiolitakis, A., and Gerlinger, P., "An implicit splitting scheme with characteristic boundary conditions for compressible reactive flows on unstructured grids," *Journal of Computational and Applied Mathematics*, Vol. 437, 2024, p. 115446.

[26] Moureau, V., Bérat, C., and Pitsch, H., "An efficient semi-implicit compressible solver for large-eddy simulations," *Journal of Computational Physics*, Vol. 226, 2007, pp. 1256–1270.

[27] Lourier, J., Stöhr, M., Noll, B., Werner, S., and Fiolitakis, A., "Scale adaptive simulation of a thermoacoustic instability in a partially premixed lean swirl combustor," *Combustion and Flame*, Vol. 183, 2017, pp. 343–357.

[28] Toro, E., and Clarke, J., "A weighted average flux method for hyperbolic conservation laws," *Proceedings of the Royal Society of London. A. Mathematical and Physical Sciences*, Vol. 423, 1989, pp. 401–418.

[29] Setzwein, F., Ess, P., and Gerlinger, P., "An implicit high-order k-exact finite-volume approach on vertex-centered unstructured grids for incompressible flows," *Journal of Computational Physics*, Vol. 446, 2021, p. 110629.

[30] Nicoud, F., and Ducros, F., "Subgrid-scale stress modelling based on the square of the velocity gradient tensor," *Flow, Turbulence and Combustion*, Vol. 62, 1999, pp. 183–200.

[31] Gerlinger, P., Möbus, H., and Brüggemann, D., "An Implicit Multigrid Method for Turbulent Combustion," *Journal of Computational Physics*, Vol. 167, 2001, pp. 247 – 276.

[32] Gerlinger, P., "Investigation of an assumed PDF approach for finite-rate Chemistry," *Combustion Science and Technology*, Vol. 175, 2003, pp. 841–872.

[33] Colin, O., Ducros, F., Veynante, D., and Poinsot, T., "A thickened flame model for large eddy simulations of turbulent premixed combustion," *Physics of Fluids*, Vol. 12, 2000, pp. 1843–1863.

[34] Charlette, F., Meneveau, C., and Veynante, D., "A power-law flame wrinkling model for LES of premixed turbulent combustion Part I: non-dynamic formulation and initial tests," *Combustion and Flame*, Vol. 131, 2002, pp. 159–180.

[35] Poinsot, T., and Lele, S., "Boundary conditions for direct simulations of compressible viscous flows," *Journal of Computational Physics*, Vol. 101, 1992, pp. 104–129.

[36] Poinsot, T., and Veynante, D., *Theoretical and Numerical Combustion*, Aquaprint, Bordeaux, France, 2012.

[37] Yoo, C., Wang, Y., Trouve, A., and Im, H., "Characteristic boundary conditions for direct simulations of turbulent counterflow flames," *Combustion Theory and Modelling*, Vol. 9, 2005, pp. 617–646.

[38] Rudy, D., and Strikwerda, J., "A nonreflecting outflow boundary condition for subsonic navier-stokes calculations," *Journal of Computational Physics*, Vol. 36, 1980, pp. 55–70.

[39] Kathrotia, T., Oßwald, P., Naumann, C., Richter, S., and Köhler, M., "Combustion kinetics of alternative jet fuels, Part-II: Reaction model for fuel surrogate," *Fuel*, Vol. 302, 2021, p. 120736.

[40] Yin, Z., and Stöhr, M., "Time–frequency localisation of intermittent dynamics in a bistable turbulent swirl flame," *Journal of Fluid Mechanics*, Vol. 882, 2020, p. A30.

[41] Grader, M., Yin, Z., Geigle, K. P., and Gerlinger, P., "Influence of flow field dynamics on soot evolution in an aero-engine model combustor," *Proceedings of the Combustion Institute*, Vol. 38, 2021, pp. 6421–6429.

[42] Daubechies, I., *Ten lectures on wavelets*, Society for industrial and applied mathematics, Philadelphia, Pennsylvania, 1992.

[43] Upatnieks, A., Driscoll, J., and Ceccio, S., "Cinema particle imaging velocimetry time history of the propagation velocity of the base of a lifted turbulent jet flame," *Proceedings of the Combustion Institute*, Vol. 29, 2002, pp. 1897–1903.

[44] Lupi, V., Canton, J., and Schlatter, P., "Global stability analysis of a 90°-bend pipe flow," *International Journal of Heat and Fluid Flow*, Vol. 86, 2020, p. 108742.